



HAL
open science

High-contrast, high-angular resolution view of the GJ 367 exoplanet system

Wolfgang Brandner, Per Calissendorff, Neige Frankel, Faustine Cantalloube

► **To cite this version:**

Wolfgang Brandner, Per Calissendorff, Neige Frankel, Faustine Cantalloube. High-contrast, high-angular resolution view of the GJ 367 exoplanet system. *Monthly Notices of the Royal Astronomical Society*, 2022, 513, pp.661-669. 10.1093/mnras/stac961 . insu-03667421

HAL Id: insu-03667421

<https://insu.hal.science/insu-03667421>

Submitted on 8 Mar 2023

HAL is a multi-disciplinary open access archive for the deposit and dissemination of scientific research documents, whether they are published or not. The documents may come from teaching and research institutions in France or abroad, or from public or private research centers.

L'archive ouverte pluridisciplinaire **HAL**, est destinée au dépôt et à la diffusion de documents scientifiques de niveau recherche, publiés ou non, émanant des établissements d'enseignement et de recherche français ou étrangers, des laboratoires publics ou privés.

High-contrast, high-angular resolution view of the GJ 367 exoplanet system

Wolfgang Brandner¹  ¹★, Per Calissendorff,² Neige Frankel^{1,3} and Faustine Cantalloube⁴

¹Max-Planck-Institut für Astronomie, Königstuhl 17, D-69117 Heidelberg, Germany

²Department of Astronomy, University of Michigan, Ann Arbor, MI 4810, USA

³Canadian Institute for Theoretical Astrophysics, University of Toronto, 60 St. George Street, Toronto, ON M5S 3H8, Canada

⁴Aix Marseille Univ, CNRS, CNES, LAM, 13388 Marseille cedex 13, France

Accepted 2022 April 4. Received 2022 March 30; in original form 2022 February 3

ABSTRACT

We search for additional companions in the GJ 367 exoplanet system and aim to better constrain its age and evolutionary status. We analyse high-contrast direct imaging observations obtained with *HST*/NICMOS, VLT/NACO, and VLT/SPHERE. We investigate and critically discuss conflicting age indicators based on theoretical isochrones and models for Galactic dynamics. A comparison of *GAIA* EDR3 parallax and photometric measurements with theoretical isochrones suggests a young age ≤ 60 Myr for GJ 367. The star's Galactic kinematics exclude membership to any nearby young moving group or stellar stream. Its highly eccentric Galactic orbit, however, is atypical for a young star. Age estimates considering Galactic dynamical evolution are most consistent with an age of 1–8 Gyr. We find no evidence for a significant mid-infrared excess in the *WISE* bands, suggesting the absence of warm dust in the GJ 367 system. The direct imaging data provide significantly improved detection limits compared to previous studies. At 530 mas (5 au) separation, the SPHERE data achieve a 5σ contrast of 2.6×10^{-6} . The data exclude the presence of a stellar companion at projected separations ≥ 0.4 au. At projected separations ≥ 5 au we can exclude substellar companions with a mass $\geq 1.5 M_{\text{Jup}}$ for an age of 50 Myr, and $\geq 20 M_{\text{Jup}}$ for an age of 5 Gyr. By applying the stellar parameters corresponding to the 50 Myr isochrone, we derive a bulk density of $\rho_{\text{planet}} = 6.2 \text{ g cm}^{-3}$ for GJ 367 b, which is 25 per cent smaller than a previous estimate.

Key words: Planets and satellites: detection – Planets and satellites: dynamical evolution and stability – Planets and satellites: formation – Planets and satellites: individual: GJ 367b – Planets and satellites: terrestrial planets – Stars: individual: GJ 367.

1 INTRODUCTION

GJ 367 is an early M-dwarf located at a distance of 9.4 pc, with a close-to-solar metallicity of $[\text{Fe}/\text{H}] \approx -0.01 \pm 0.12$. It is host to GJ 367b, a transiting exoplanet with a 7.7 h orbital period, corresponding to a semimajor axis of ≈ 0.007 au (≈ 0.75 mas maximum projected separation for a circular orbit). With an estimated radius of $0.72 R_{\text{Earth}}$ and mass of $0.55^{+0.03}_{-0.04} M_{\text{Earth}}$, GJ 367b is currently the smallest and lowest mass exoplanet known within 10 pc of the Sun. The implied density of 8.2 g cm^{-3} classifies it as a rocky planet with an extended, iron dominated core. With a dayside equilibrium temperature of 1500–1750 K, GJ 367b classifies as a lava planet (Lam et al. 2021).

The host star GJ 367 is showing no signs of strong variability or activity. Photometric monitoring covering 5 yr, and comprising 11 distinct observing epochs, derived a *V*-band variability amplitude of 12 mmag (Hosey et al. 2015). GJ 367's activity index of $R'_{\text{HK}} = -5.15 \pm 0.12$ and rotational period of $P_{\text{rot}} = 53$ d (Astudillo-Defru et al. 2017) closely follow the relation typical for relatively quiet early M-dwarfs (Suárez Mascareño et al. 2015). One peculiarity of

GJ 367 is its high space motion with respect to the Sun. As recently as 130 000 yr ago, the Sun and GJ 367 had their closest encounter at a perihelion distance of ≈ 5.4 pc (Bailer-Jones et al. 2018). An analysis combining *HIPPARCOS* and *GAIA* EDR3 astrometry of GJ 367 finds a 3.8σ significance for a proper motion anomaly, possibly indicating the presence of a substellar companion (Kervella, Arenou & Thévenin 2022). The *GAIA* EDR3 astrometric excess noise, which is the noise to be added to the individual *GAIA* observations to achieve a reduced χ^2 of 1 in the astrometric fit of the single star model (Lindegren et al. 2018), has a significance of $\approx 17\sigma$ (Gaia Collaboration et al. 2016, 2021).

The proximity to the Sun and the EDR3 astrometric anomaly make GJ 367 an interesting target for a direct imaging search for companions at projected separations $\gtrsim 1$ au.

The outline of the paper is as follows: In section 2, we present the high-angular resolution data and their analysis. In section 3, we investigate various age indicators and the Galactic kinematics. In section 4, we discuss the findings and identify four challenges towards a better understanding of the GJ 367 exoplanet system.

* E-mail: brandner@mpia.de

2 OBSERVATIONS AND DATA REDUCTION

We identified three high angular and high contrast observations of GJ 367 in the Mikulski Archive for Space Telescopes and the archive of the European Southern Observatory (see Table 1).

2.1 HST/NICMOS

GJ 367 was observed with *HST*/NICMOS (Thompson & Schneider 1998) as part of a snapshot survey for companions to nearby stars (see Table 1 for observational details). The filter combination had been selected to provide a differentiator between background stars and substellar companions with CH₄ absorption bands (Dieterich et al. 2012).

We detect five companion candidates (cc) to GJ 367 in all four bands of the NIC2 data set (see Fig. 1, left-hand panel, cc1–cc5, and Table 2). *GAIA* parallax measurements and upper limits identify four of these sources as background objects. The brightest source cc2 was already classified as a background dwarf star based on its F110W - F222M colour by Dieterich et al. (2012). The 5th and faintest source cc3 has no counterpart in EDR3. The fact that it is detected in all 4 NIC2 filters suggests the absence of CH₄ absorption bands, thus it is most likely also an unrelated background source.

Dieterich et al. (2012) provide radial detection limits in F180M, which reach 3–5 σ contrast ratios $\gtrsim 2.4 \times 10^4$ for angular separations $\geq 3''$. The *HST*/NIC2 radial contrast limits for separations $\leq 2''$ ($\lesssim 20$ au projected separation) are included in Fig. 3.

2.2 VLT/NACO

GJ 367 was observed with VLT/NACO (Lenzen et al. 2003; Rousset et al. 2003) as part of a programme to probe for stellar multiplicity among nearby low mass stars (see Table 1). The observations were carried out during a period of very low ground-level winds ($\langle v_{\text{wind}} \rangle = 0.37 \pm 0.19 \text{ m s}^{-1}$). The resulting low-wind effect is known to create phase shifts in the wavefront in specific quadrants of the telescope pupil, resulting in one or multiple (transient) side-lobes of point sources (Sauvage et al. 2016; Milli et al. 2018). We reduced the data with the EsoRex NACO pipeline Version 4.4.10. Fig. 1 (right-hand panel) shows the coadded image. The inset on the lower left shows, as an example, one of several individual frames affected by the low-wind effect. The inset in the lower right shows the coadded frame. The side-lobe is much less pronounced, yet still visible as a diffuse “smudge” to the upper left of the PSF centre.

Compared to the shortest wavelength *HST*/NIC2 observations, the VLT/NACO observations have a two times finer diffraction-limited resolution. The data confirm that GJ 367 is unresolved (i.e. not a stellar binary) down to a projected separation of ≈ 0.4 au (Fig. 1, right-hand panel).

We also carried out a visual search for companion candidates. No other sources were detected down to $m_{\text{NB175}} \approx 13.5$ mag (i.e. about 7.5 mag fainter than GJ 367). cc1, which is about 10.1 mag fainter than GJ 367 in *GAIA* BP and RP, and like GJ 367 has *GAIA* BP - RP ≈ 2.3 mag, is below the detection limit of the VLT/NACO data set.

2.3 VLT/SPHERE

GJ 367 was observed with VLT/SPHERE (Beuzit et al. 2019) as part of a programme to probe for substellar companions to nearby stars (see Table 1). The pupil stabilized angular differential imaging (ADI Marois et al. 2006) observing sequence was obtained with the apodized Lyot coronagraph (Martinez et al. 2009; Carillet et al.

2011; Soummer et al. 2011). Before the start and after the end of the coronagraphic observing sequence, a single data set with the satellite spots turned on was recorded in order to facilitate the estimation of the star centre position behind the coronagraph. During the ADI sequence, the satellite spots were not present.

We reduced the data using a combination of the EsoRex SPHERE pipeline version 0.42.0 and the vlt-sphere python package version 1.4.3 (Vigan 2020).¹ For the astrometric calibration (i.e. image plate scale and orientation), we adopted the values by Maire et al. (2016).

A point source cc6 is detected (Fig. 2, left-hand panel, and Table 2) in the IRDIS H2 ($\lambda_c = 1589$ nm) and H3 ($\lambda_c = 1667$ nm) bands. This source has no counterpart in EDR3. Compared to GJ 367, cc6’s H2-H3 colours are ≈ 0.1 mag redder. Thus, most likely it is a background star of a slightly later spectral type than GJ 367. Due to the high proper motion of GJ 367, there is no overlap between the field of view of NIC2 in 1997 and IRDIS in 2020.

The resulting pre-reduced four-dimensional (4D) (x , y , time, wavelength) IRDIS and IFS data sets were further processed with ANDROMEDA version 3.1 (Cantalloube et al. 2015). Fig. 2 (right-hand panel) shows the resulting residual after spectral ADI (SADI) processing of the IRDIS data. No close companion candidate was detected. Fig. 3 shows the radial contrast curve (red dashed line) for our SADI analysis of the SPHERE/IRDIS dual-band imaging data. In the central 700 mas (≈ 6.6 au projected separation), the IFS and IRDIS contrast curves after SADI processing are quite similar. VLT/SPHERE achieves a 5 σ contrast of $\approx 2.6 \times 10^{-6}$ at 5 au (520 mas) and $\approx 1 \times 10^{-6}$ beyond 14 au (1500 mas). The *HST*/NIC2 contrast curve (black dotted line) according to Dieterich et al. (2012) is overplotted for reference.

3 AGE AND FORMATION HISTORY OF GJ 367

The age determination presents the main challenge in converting the contrast ratio between a substellar companion and its host star into a mass estimate. Primary age indicators are the evolutionary state of the star, its activity and rotational period, and Galactic kinematics (Soderblom 2010).

3.1 Isochronal age and metallicity

The proximity of GJ 367 results in precise parallax measurements, and hence a precise determination of its absolute magnitudes. Table 3 presents a compilation of optical and infrared photometry of GJ 367. Its metallicity is close to solar (Lam et al. 2021), which makes theoretical isochrones computed for solar metallicity directly applicable (see Table 4 for a compilation of recent metallicity estimates). In Fig. 4, left-hand panel, we compare GJ 367’s absolute *GAIA* BP magnitude and *GAIA* BP - RP colour with theoretical isochrones by Baraffe et al. (2015). Under the assumption that GJ 367 is a single star, the isochrones suggest an age of around 55–60 Myr. Isochrones in the 2MASS photometric system, on the other hand, do not provide an age discriminant. This is in part due to the larger photometric uncertainties of the 2MASS measurements, and in part due to the fact that the isochrones in the 2MASS system are degenerate² for

¹<https://github.com/avigan/SPHERE>

²As pointed out by Allard & Hauschildt (1995), for late-type dwarfs of solar metallicity, molecular opacities lock in place the peak of the flux at $\approx 1.1 \mu\text{m}$ over a broad range of effective temperatures. Thus the flux in the visual provides a better diagnostics on effective temperature and evolutionary state.

Table 1. Basic parameters of high contrast observations of GJ 367.

Telescope/instrument	<i>HST</i> /NICMOS	VLT/NACO	VLT/SPHERE	
Camera	NIC2	S13	IFS	IRDIS
Field of view [″ × ″]	19.4 × 19.4	13.6 × 13.6	1.73 × 1.73	11.0 × 12.5
Image scale [mas/pixel]	75.65	13.25	7.46	12.25
Filter/wavelength range	F110W, F180M, F207M, F222M	F185N	YJ	H2+H3
Angular resolution [mas]	≥95	48	≥25*	≥41*
Total integration time [s]	64, 64, 128, 128	280	3136	2816
Integration set-up	STEP64, STEP64, STEP128, STEP128	0.5s × 20 × 28	32s × 1 × 98	8.0s × 2 × 176
Telescope tracking	stare	Auto-jitter	Pupil stabilized	
Programme ID	GO 7420	70.C-0738(A)	0104.C-0336(A)	
Principal Investigator	David A. Golimowski	Jean-Luc Beuzit	Anna Boehle	
Observing date	1997-09-17	2003-03-17	2020-02-08	
Remarks	Snapshot	Low wind effect	ADI + Lyot coronagraph	

Note. *Inner working angle ≈150 mas with apodized Lyot coronagraph.

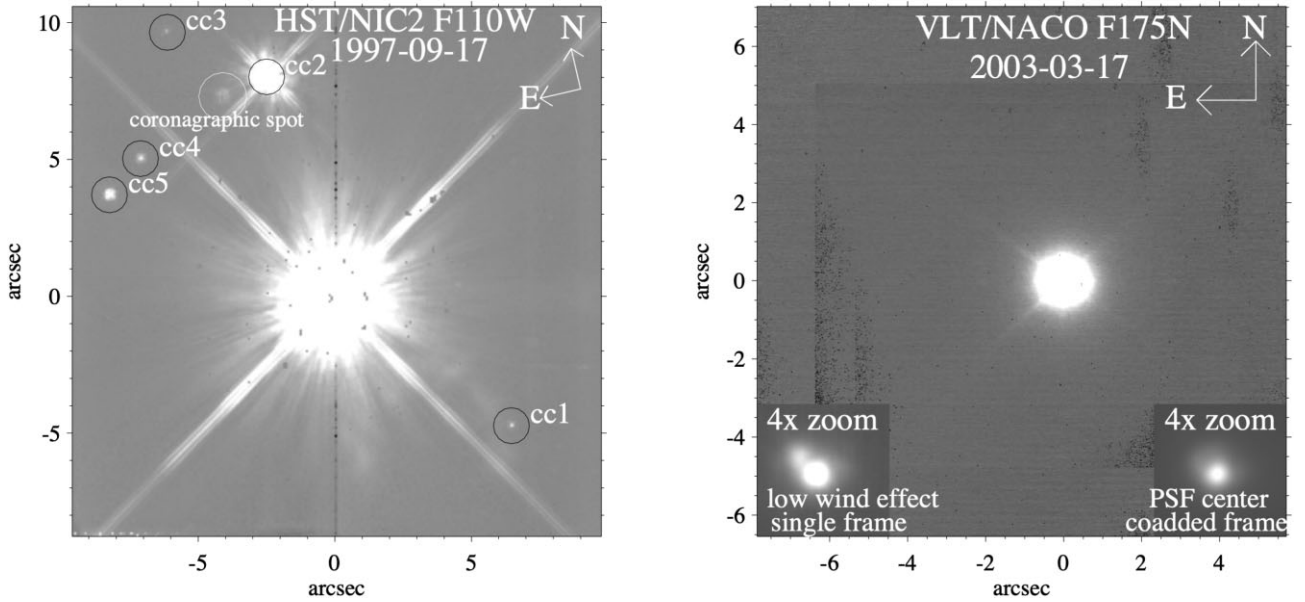


Figure 1. Left-hand panel: *HST* NIC2 image in F110W centred on GJ 367, with five cc visible (black circles). The location of residuals originating in NIC2’s coronagraphic mask is indicated (white circle). Right-hand panel: VLT/NACO image in NB175 centred on GJ 367. The lower left inset shows a 4× zoom-in on an individual 10 s frame depicting a side-lope resulting from the low wind effect. The inset on the lower right shows a 4× zoom-in of the coadded PSF.

Table 2. Companion candidates (cc) to GJ 367.

ID	Epoch	sep [″]	PA [°]	Δmag [mag]	Status	GAIA EDR3 ID
cc1	1997-09-17	8.03	222.2	11.46 (F110W)	Non-common proper motion	5412250575032741504
cc2	1997-09-17	8.45	3.1	3.39 (F110W)	Non-common proper motion	5412250575040992256
cc3	1997-09-17	11.54	18.9	11.95 (F110W)	Background star (no CH ₄ absorption)	–
cc4	1997-09-17	8.72	40.7	10.07 (F110W)	Non-common proper motion	5412250575040992768
cc5	1997-09-17	9.05	51.8	8.44 (F110W)	Non-common proper motion	5412250540683548160
cc6	2020-02-08	6.48	39.8	11.13 (H2)	Background M-dwarf (H2-H3 colour)	–

Note. Separation “sep” and Position Angle “PA” are measured relative to GJ 367 in the epoch of the respective high-contrast observations.

objects of GJ 367’s near-infrared colours and magnitudes (Fig. 4, right-hand panel). Thus, we consider the isochronal age estimate of $8.0^{+3.8}_{-4.6}$ Gyr by Lam et al. (2021), which is based on the *GAIA* DR2 parallax and the 2MASS photometry, of limited informative value.

A comparison of GJ 367’s location in a *GAIA* Colour–magnitude diagram with the other ≈150 M dwarfs within 10 pc of the Sun (using

the sample defined by Stelzer et al. 2013) reveals that its colour and magnitude is rather typical (i.e. average) for an early M-dwarf (Fig. 4, left-hand panel). The dispersion in absolute magnitudes above the (solar metallicity) main sequence for nearby late K- and early M-type stars can in part be explained by unresolved binary stars (Zari et al. 2018), and in part by a spread in metallicity above solar.

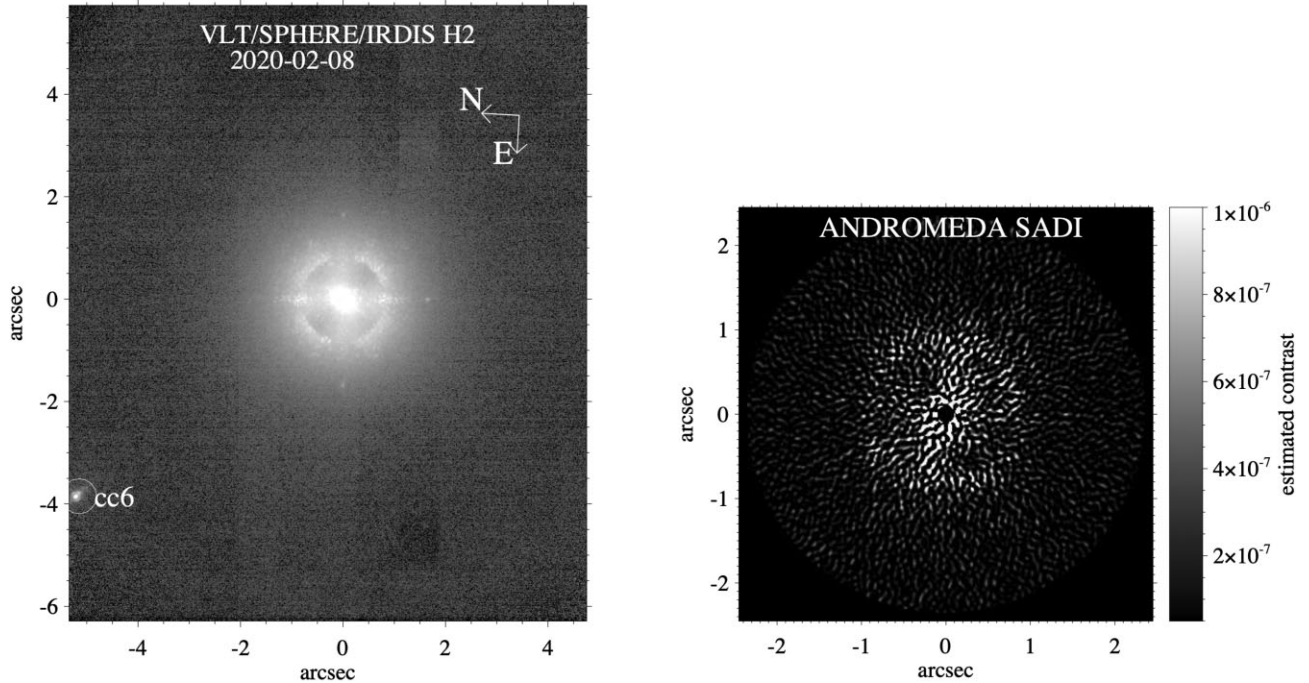


Figure 2. Left-hand panel: the companion candidate cc6 is detected at the very edge of the IRDIS field of view. Right-hand panel: map of the estimated contrast for the IRDIS H2+H3 observations following SADI processing with ANDROMEDA, based on the assumption that a point source would be located at this pixel position.

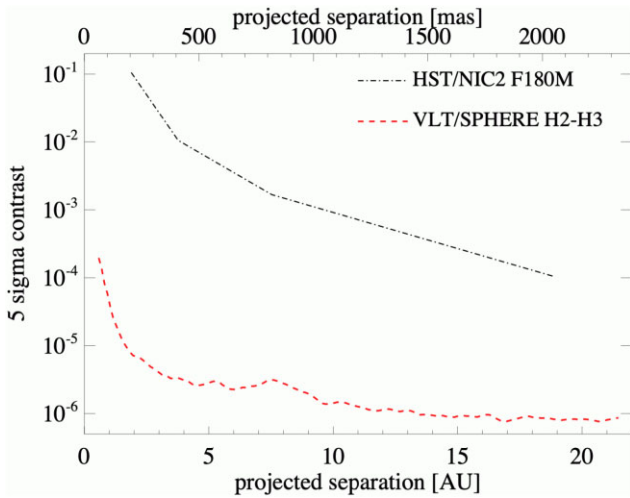


Figure 3. Radial 5σ contrast achieved with NIC2 in the F180M filter [dash-dotted line, Dieterich et al. (2012)] and SADI processed SPHERE/IRDIS in the H2/H3-filters (red dashed line) plotted over the projected separation.

By being about 0.5 mag brighter in the optical and near-infrared than the 1–10 Gyr solar-metallicity main sequence, GJ 367’s location in the colour–magnitude diagram coincides with the binary sequence. Our direct imaging data exclude a stellar companion at projected separations ≥ 0.4 au in the 2003 data set, and at projected separations ≥ 1 au in the data sets obtained in 1997 and 2020. We also found no evidence in the literature for GJ 367 having a closer-in stellar companion (i.e. no hint for a spectroscopic, astrometric, or eclipsing binary).

In order to investigate the effect of the uncertainty in the metallicity of GJ 367 (Table 4) on the isochronal age estimate, we use the Mesa

Table 3. Compilation of (apparent) optical, near-, and mid-infrared photometry, distance modulus (DM), and absolute flux (i.e. at 10 pc distance) of GJ 367.

Band	[mag]	λF_{λ} [10^{-12} W m $^{-2}$]	Source
G_{BP}	10.3735 ± 0.0008	1.346 ± 0.002	EDR3
G	9.1587 ± 0.0003	3.069 ± 0.002	EDR3
G_{RP}	8.0582 ± 0.0005	4.959 ± 0.003	EDR3
J	6.632 ± 0.023	7.635 ± 0.007	2MASS
H	6.045 ± 0.044	6.26 ± 0.13	2MASS
K_s	5.780 ± 0.020	4.00 ± 0.17	2MASS
W1	5.550 ± 0.164	1.459 ± 0.027	AllWISE
W2	5.364 ± 0.061	0.71 ± 0.12	AllWISE
W3	5.477 ± 0.015	0.045 ± 0.003	AllWISE
W4	5.381 ± 0.038	0.0071 ± 0.0001	AllWISE
DM	$-0.13006^{+0.00058}_{-0.00029}$	–	EDR3

Note. References: EDR3 - GAIA Collaboration et al. (2021); 2MASS - Cutri et al. (2003); and AllWISE - Cutri et al. (2021)

Table 4. Compilation of metallicity estimates of GJ 367.

[Fe/H]	Reference
-0.07 ± 0.09	Kuznetsov et al. (2019)
-0.06 ± 0.09	Maldonado et al. (2019)
-0.01 ± 0.12	Lam et al. (2021)

Isochrones and Stellar Tracks (MIST, Dotter 2016) in the GAIA EDR3 photometric system and for $[\text{Fe}/\text{H}] = (-0.25, 0.00, +0.25)$. To account for the long rotational period of GJ 367, we selected the isochrones for $\nu/\nu_{\text{crit}} = 0.0$. For $[\text{Fe}/\text{H}] = 0.0 \pm 0.25$, we derive an isochronal age of 28^{+35}_{-17} Myr for GJ 367. In general, sub-solar metal-

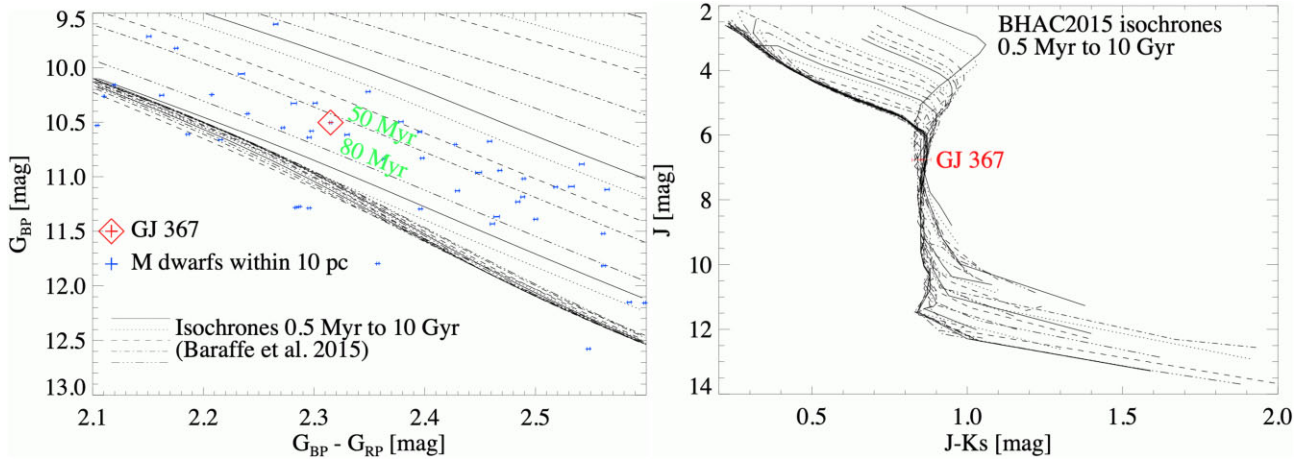


Figure 4. Colour–magnitude diagrams for GJ 367 compared to theoretical models by Baraffe et al. (2015). The left-hand panel shows isochrones in the *GAIA* photometric systems, with GJ 367 (red symbol) being located below the 50 Myr and above the 80 Myr isochrone. The right-hand panel illustrates that isochrones transformed to 2MASS bands do not provide any meaningful constraint on GJ 367’s age. The 1σ error bars in both plots are based on the uncertainties in photometry and parallax.

licity isochrones suggest a younger age, and super-solar metallicity isochrones yield an older age.

According to the MIST models, a 1–10 Gyr old early M-dwarf with a metallicity of $[\text{Fe}/\text{H}] \approx +0.45$ would fit GJ 367’s optical and near-infrared luminosity. Such a high metallicity, though, deviates by at least 4σ from GJ 367’s close-to-solar metallicity estimates.

3.2 Mid-infrared emission

Bentley et al. (2019) investigated *GAIA*, 2MASS, and *WISE* photometry of $\approx 100\,000$ nearby M-dwarfs. With $G-J = 2.53$ mag and $G-K = 3.38$ mag, GJ 367’s *GAIA* and 2MASS colours are typical for M1 to M2 dwarfs. Compared to early M-dwarfs in the ≥ 500 Myr old field star sample, though, GJ 367’s reveals a 2–3 σ infrared excess in the *WISE* bands ($K-W2 = 0.42$ mag, $W1-W2 = 0.19$ mag, see Table 3). We also compare the spectral energy distribution of GJ 367 with models for a $0.4 M_{\odot}$ star by Baraffe et al. (2015). According to the models, the $0.4 M_{\odot}$ star has $T_{\text{eff}} = 3512$ K at an age of 50 Myr, and $T_{\text{eff}} = 3521$ K at an age of 5 Gyr, which is a very good match to the $T_{\text{eff}} = 3522 \pm 70$ K reported by Lam et al. (2021). While the 50 Myr model provides a good fit to the photometry of GJ 367, the 5 Gyr model predicts only about 65 per cent to 70 per cent of its observed optical, near- and mid-infrared flux.

3.3 Gyrochronology and age

Gyrochronology relies on the assumption that young stars at the end of their contraction phase arrive on the main sequence with high angular momentum, and subsequently are able to lose angular momentum by stellar winds. Main-sequence stars with longer rotational periods should thus be on average older than main sequence stars with shorter rotational periods. This then facilitates age-dating of a main-sequence star from its rotational period (Mamajek 2012).

Based on photometric monitoring data, Lam et al. (2021) deduced a rotational period of 48 ± 2 d for GJ 367, which is consistent with the rotational period of $P_{\text{rot}} = 53$ d according to Astudillo-Defru et al. (2017). Lam et al. (2021) derived a gyrochronological age of 4.0 ± 1.1 Gyr.

For early M-dwarfs, a study of single and multiple stars in the Hyades finds a significant dearth of rapid rotators around single

Table 5. GJ 367’s Galactic coordinates and velocities in a left-handed coordinate system (not corrected for LSR).

XYZ [pc]	0.3667, -9.3621 , 0.9289
UVW [km s^{-1}]	-3.27 , -50.87 , -28.30

Note. Based on positions, parallax and proper motions from *GAIA* EDR3, radial velocity according to Trifonov et al. (2020), and the transformation matrix defined in ESA (1997).

stars with masses $\geq 0.3 M_{\odot}$ (Douglas et al. 2016). Single Hyades members from the sample defined by Kopytova et al. (2016) with masses of $\approx 0.4 M_{\odot}$ have a typical rotational period of ≈ 20 d, which is about three times longer than predicted by models of the angular momentum evolution of low mass stars (Reiners & Mohanty 2012). According to Douglas et al. (2016), this suggests that for single stars with undisturbed circumstellar discs, magnetic braking might be a highly efficient mechanism to shed angular momentum. As a consequence, the rotational period of early M-dwarfs might have less informative power as an age indicator.

3.4 Galactic kinematics and moving groups membership

We base our investigation of GJ 367’s Galactic kinematics on *GAIA* EDR3 positions, parallax and proper motions, and on the weighted mean radial velocity of $RV = 47.9216 \pm 0.0001$ km s^{-1} from the public HARPS data base corrected for systematics (Trifonov et al. 2020). The transformation from the *GAIA* EDR3 observables in the International Celestial Reference System (ICRS) to XYZ positions and UVW velocities (see Table 5) in a left-handed Galactic reference frame (U positive for motions towards the Galactic anti-centre) is based on the transformation matrix defined in ESA (1997). The resulting values are $U = -3.3$ km s^{-1} , $V = -50.9$ km s^{-1} , and $W = -28.3$ km s^{-1} . This is in very good agreement with Lam et al. (2021) [$U_{\text{LSR}}, V_{\text{LSR}}, W_{\text{LSR}} = (-11.73 \pm 0.01, -36.5 \pm 0.4, -21.93 \pm 0.04)$], when assuming that they based their correction to the local standard of rest (LSR) on Coşkunoğlu et al. (2011), i.e. $U_{\odot}, V_{\odot}, W_{\odot} = -8.50$,

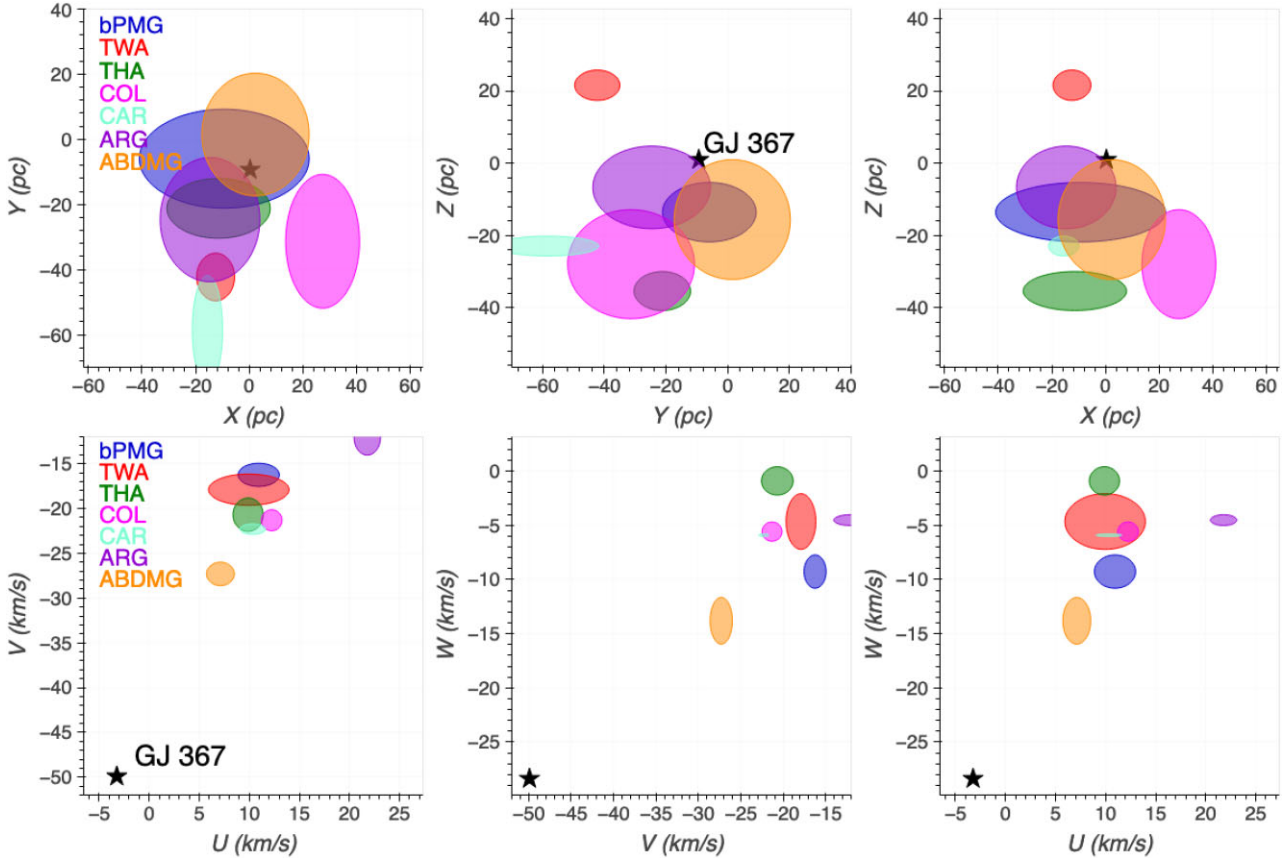


Figure 5. XYZ coordinates and UVW velocities of GJ 367 compared to Young Moving Groups in a left-handed Galactic coordinate system [graphics adapted from Rodriguez (2016)].

13.38, 6.49 km s⁻¹ in a left-handed coordinate system (thus the minus sign in U_{\odot}).³

Fig. 5 illustrates that GJ 367’s kinematics differ significantly from those of nearby young moving groups (Malo et al. 2013), and hence excludes membership to any of these groups. GJ 367’s UVW velocities are also distinct from those of the Hercules stream (see, e. g. Chen et al. 2021). This finding is supported by the LACEWING (Riedel et al. 2017) and BANYAN (Gagné et al. 2018) analysis tools for assessing membership to nearby young moving groups. Thus, GJ 367 is not a member of any nearby moving group or stream.

3.5 Age constraints from Galactic dynamics

The birth conditions and subsequent evolutionary history of stellar populations determine their present-day Galactic kinematics and

³We note that Lam et al. (2021)’s choice of LSR correction results in a small inconsistency when they assess the likelihood for GJ 367’s membership to the different Galactic populations according to Bensby, Feltzing & Lundström (2003). The latter report U_{LSR} , V_{LSR} , W_{LSR} for thin and thick disc, and halo stars in a right-handed coordinate system, and based on a solar motion with respect to the LSR of U_{\odot} , V_{\odot} , $W_{\odot} = (10.00, 5.25, 7.17)$ km s⁻¹ according to Dehnen & Binney (1998). As Bensby et al. (2003) assume Gaussian probability distributions functions for the populations depending on the square of the UVW velocities, the choice of right- or left-handed coordinate system does not affect the likelihood estimate, though the difference in particular in V_{\odot} results in $\Delta V_{\text{LSR}} \approx 8$ km s⁻¹.

metallicity. Frankel et al. (2018) and Frankel et al. (2020) constructed a global model for the distribution of stars’ [Fe/H], ages, positions, and velocities, and fitted it to APOGEE DR12 and DR14 data. Here, we use this model to produce an age posterior for the star, given its [Fe/H] and kinematics.

Noteworthy are GJ 367’s V and W components, i.e. the velocity component parallel to the Galactic plane and perpendicular with respect to the Galactic centre, and the velocity component vertical to the Galactic plane. Relative to the Sun, GJ 367’s V component is ≈ 50 km s⁻¹ less, and thus considerably slower than the circular velocity at the position of the Sun. This indicates a Galactic orbit with a significant eccentricity.

We used galpy v1.7.1 (Bovy 2015) to integrate GJ 367’s orbit with the MWPotential2014 Galactic potential. Fig. 6 shows the results of the integration in the radial-vertical plane. We selected the following plausible input parameters: $R = 8.12$ kpc (Gravity Collaboration et al. 2018), $v_{\text{T}} = -14.5$ km s⁻¹, $v_{\text{R}} = 198$ km s⁻¹, $z = 22$ pc, $v_z = -21$ km s⁻¹. According to the orbit integration, the pericentre and apocentre of GJ 367’s orbit are at ≈ 5.65 and ≈ 8.15 kpc, corresponding to an eccentricity $e \approx 0.3$.⁴

The following analysis (Fig. 7) is along the lines of the investigation carried out in order to age-date the HD 19467 system (Maire et al. 2020). It is based on the latest version of the Galactic models

⁴We aim at a qualitative analysis. Quantitative estimates will vary according to the precise choice of the LSR correction.

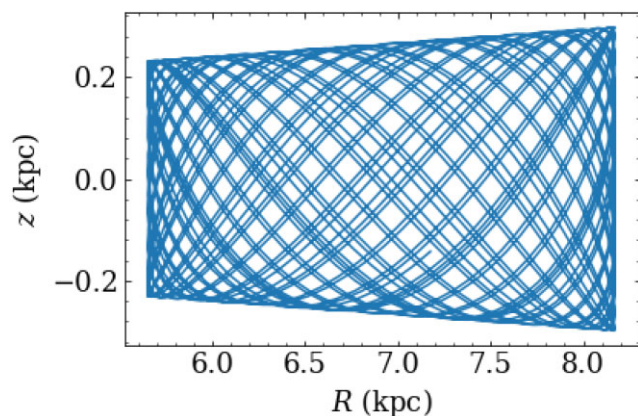


Figure 6. Vertical-radial projection of multiple Galactic orbits of GJ 367. At the solar circle, GJ 367 is close to its apocentre, with the pericentre corresponding to $R \approx 5.65$ kpc. GJ 367 oscillates with an amplitude of ± 240 to ± 280 pc vertical to the Galactic plane.

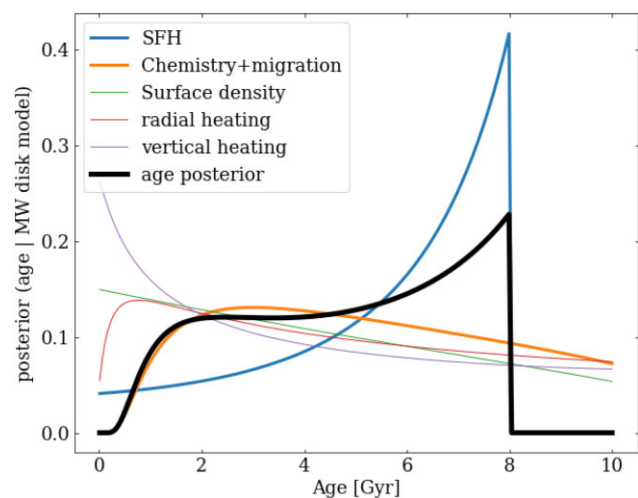


Figure 7. Posterior age of GJ 367 based on $[\text{Fe}/\text{H}]$, Galactic angular momentum, radial action, and height above the Galactic plane (thick black). Contributions from individual model components entering the posterior are re-normalized and over-plotted according to the legend: star formation history and radial surface density, chemical information, orbital heating.

as described in Frankel et al. (2020). The analysis derives an age posterior considering (1) the Galactic star formation history (SFH), (2) the chemical and migration model (i.e. the stellar metallicity and position), (3) the surface density of stars, (4) the radial heating, which is reflected in the eccentricity of the stellar orbit, and (5) the vertical heating, i.e. the average height of the star above the Galactic plane.

The most influential contributions are (i) the star formation history of the low- α disc, which describes that there are more old than young stars; (ii) the chemical+migration model, which – given this star’s metallicity and position – provides a range of possible birthplaces and birth times. If there were no radial migration in the Milky Way, this would be the most constraining parameter. For GJ 367, it shows a broad and flat peak between 1.5 and 4 Gyr. Thus, the star formation history still dominates the posterior.

Another aspect is the (currently) low vertical height of the star. As a consequence, the vertical secular evolution model favours a young

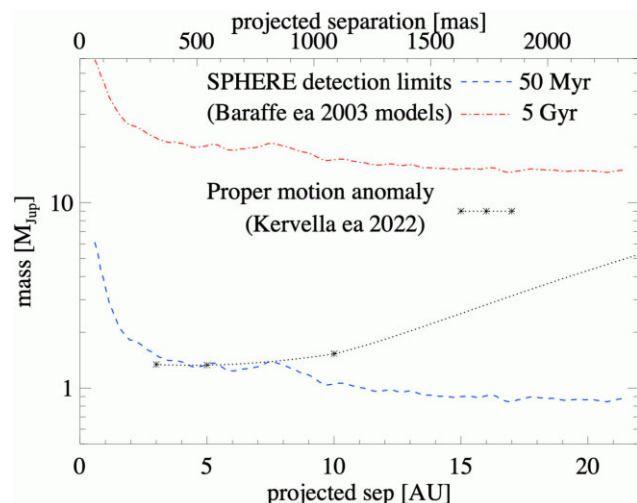


Figure 8. Radial mass detection limits for SPHERE, transformed from 5σ contrast limits using the models by Baraffe et al. (2003) for ages of 50 Myr (blue dashed line) and 5 Gyr (red dashed-dotted line). The asterisk symbols and the dotted line mark the companion mass-to-orbital radius relation, explaining the proper motion anomaly of GJ 367 according to Kervella et al. (2022).

age. The eccentricity, on the other hand, is quite large. Thus, the in-plane secular evolution favours an older age.

Overall, the disc model produces a very broad posterior for the age of the star, with probable values between 1 and 8 Gyr. The chemodynamical aspects of the model tend to favour a young age, whereas the global star formation history aspect draws the posterior to an older age. Utilizing additional chemical information in the future (e.g. including alpha element abundances) may help constraining the age further.

4 DISCUSSION

The VLT/SPHERE observations provide significantly improved detection limits compared to previous direct imaging observations of the GJ 367 system. The corresponding companion mass detection limits according to models by Baraffe et al. (2003) for ages of 50 Myr and 5 Gyr are shown in Fig. 8. The presence of a massive brown dwarf companion is excluded, even for relatively old system ages. For a young system age, the observations would have been sufficiently sensitive to detect a $1.5 M_{\text{Jup}}$ planet at a projected separation of 5 au. This could help to narrow down the parameter range of possible companion masses and separations calculated by Kervella et al. (2022). According to their study, the *HIPPARCOS-GAIA* EDR3 proper motion anomaly would require a companion with a mass $\geq 1.5 M_{\text{Jup}}$ orbiting with a semimajor axis ≥ 10 au, or a companion with a mass $\approx 1.3 M_{\text{Jup}}$ orbiting with a semimajor axis $\lesssim 5$ au (see Fig. 8).

The exoplanet host GJ 367 provides contradicting age indicators (Table 6). Its intrinsic over-luminosity compared to 1–10 Gyr old early M-dwarfs of solar metallicity suggests a maximum age of 60 Myr.

Direct imaging observations rule out blending with a background star, or a stellar companion in a wider ($\gtrsim 1$ au) orbit. Radial velocity monitoring also rules out a closer-in stellar companion as an explanation for the over-luminosity. Metallicity measurements rule out the high metallicity of $[\text{Fe}/\text{H}] \approx +0.45$ required according to the

Table 6. Age estimators for GJ 367.

Method	Age [Myr]	Reference
Isochrones: BHAC ^a	57 ⁺³ ₋₂	This paper
Isochrones: MESA ^b	28 ⁺³⁵ ₋₁₇	This paper
Gyrochronology	3980 ± 1110	Lam et al. (2021)
Galactic Dynamics ^c	5500 ⁺²⁵⁰⁰ ₋₄₅₀₀	This paper

Notes. ^aassuming solar metallicity for GJ 367; ^bassuming $-0.25 \leq [\text{FeH}] \leq +0.25$ for GJ 367; ^cassuming that GJ 367's space motion is the result of many low momentum exchange encounters, and not dominated by a single, high momentum exchange n -body interaction. Note: given the spread of age estimates, we decided to choose 50 Myr and 5 Gyr as exemplary ages for the conversion of contrast limits into mass limits.

MIST models for a 1–10 Gyr old early M-dwarf to match GJ 367's *GAIA* EDR3 parallax and photometric measurements.

GJ 367's Galactic kinematics, and in particular the eccentricity of its Galactic orbit are well explained by Galactic dynamical evolution over a time period of 1–8 Gyr. Such an age is in agreement with the gyrochronological age, but in conflict with the isochronal age. Future studies of the $[\alpha/\text{Fe}]$ abundance of GJ 367 might provide more stringent constraints on its membership to a particular Galactic stellar population.

An alternative explanation for the eccentricity of GJ 367's Galactic orbit would be a fairly recent high-energy gravitational encounter, which changed its Galactic orbital parameters. This encounter could have happened early in the youth of GJ 367, and would point to its formation in a non-hierarchical multiple system, or a relatively dense cluster environment. While we cannot distinguish between these two scenarios, there is a high probability that either event would have significantly disturbed the orbits of any potential companions to GJ 367. This would be one explanation for GJ 367 lacking companions in wide orbits. In general, the formation environment leaves an imprint on the architecture of planetary systems (Winter et al. 2020).

In the following we identify four challenges. Their solution might provide a better understanding of the age and evolutionary history and status of the GJ 367 exoplanet system.

- (i) Challenge 1: can GJ 367 be overluminous, and not be young?
- (ii) Challenge 2: can magnetic braking explain the long rotational period of 50 d for an early M dwarf with an age ≤ 60 Myr?
- (iii) Challenge 3: does the integration of GJ 367's Galactic orbit back in time by 60 Myr hint at a possible birthplace in a non-hierarchical multiple system, or a relatively dense stellar cluster?
- (iv) Challenge 4: does the EDR3 astrometric excess noise hint at the presence of another substellar objects in the GJ 367 system? Or is the astrometric excess noise related to the limitation of the single star linear astrometric fit in EDR3, and GJ 367's proximity and peculiar space motion with respect to the Sun?⁵

Significantly deeper direct imaging detection limits might have to wait for the next generation of telescopes and instruments. Contrast ratios of a few times 10^{-9} as envisioned for the Roman Space Telescope and its Coronagraph Instrument (Trauger et al.

⁵After correcting for the projection of linear proper motion on to the celestial sphere, Brandt (2021) finds a good agreement between GJ 367's proper motion derived from *GAIA* EDR3 and HIPPARCOS positions, and the *GAIA* EDR3 proper motion.

2016; Kasdin et al. 2020; Carrión-González et al. 2021) could push detection limits to sub-Saturn mass planets.⁶

An application of the stellar parameters according to the models by Baraffe et al. (2015) (BHAC) for an age of 50 Myr changes the dependent properties of GJ 367 b. The best-fitting stellar model has a mass of $0.4 M_{\odot}$, $T_{\text{eff}} = 3512$ K, and $r_{\text{star}} = 0.479 R_{\odot}$. While the effective temperature agrees very well with the value determined by Lam et al. (2021), the models describe a star with a 5 per cent larger radius, and a 10 per cent lower mass. An increase in the planetary radius from 0.72 to $0.75 R_{\text{Earth}}$, and a decrease in the planetary mass from 0.55 to $0.48 M_{\text{Earth}}$ would result in a ≈ 25 per cent decrease in the bulk density to $\rho_{\text{planet}} = 6.2 \text{ g cm}^{-3}$ for GJ 367 b.

Irrespective of its age, GJ 367 b is a benchmark rocky planet in the solar neighbourhood. While the semimajor axis of ≈ 0.007 au of GJ 367 b is too close to its host star for direct imaging observations, phase curve and primary and secondary transit measurements should provide interesting insights into its day- and night-side properties. At a young age, the entire surface of GJ 367 b might still be covered by lava, while at an older age the nightside might have cooled below the melting point. Thus, the day- to night-side temperature contrast of GJ 367 b could serve as another age indicator for the system. At a young age, GJ 367 b could also serve as a template to Earth's Hadean period (Bonati et al. 2019).

ACKNOWLEDGEMENTS

We thank H. Zinnecker for helpful comments on a draft of the paper.

Based on observations collected at the European Organisation for Astronomical Research in the Southern Hemisphere under ESO programmes 70.C-0738(A) and 0104.C-0336(A).

Based on observations made with the NASA/ESA *Hubble Space Telescope* (GO 7420), obtained from the data archive at the Space Telescope Science Institute. STScI is operated by the Association of Universities for Research in Astronomy, Inc. under NASA contract NAS 5-26555.

This work has made use of data from the European Space Agency (ESA) mission *Gaia* (<https://www.cosmos.esa.int/gaia>), processed by the *Gaia* Data Processing and Analysis Consortium (DPAC, <https://www.cosmos.esa.int/web/gaia/dpac/consortium>). Funding for the DPAC has been provided by national institutions, in particular the institutions participating in the *Gaia* Multilateral Agreement.

This publication makes use of data products from the Two Micron All Sky Survey, which is a joint project of the University of Massachusetts and the Infrared Processing and Analysis Center/California Institute of Technology, funded by the National Aeronautics and Space Administration and the National Science Foundation.

This publication makes use of data products from the Wide-field Infrared Survey Explorer, which is a joint project of the University of California, Los Angeles, and the Jet Propulsion Laboratory/California Institute of Technology, funded by the National Aeronautics and Space Administration.

NF was supported by the Natural Sciences and Engineering Research Council of Canada (NSERC) [funding reference number CITA 490888-16] through the CITA postdoctoral fellowship and acknowledges partial support from an Arts & Sciences Postdoctoral Fellowship at the University of Toronto.

⁶GJ 367 might be on the faint side of stars accessible by the Roman Coronagraph Instrument.

DATA AVAILABILITY

The data underlying this article are available online from the Barbara A. Mikulski Archive for Space Telescopes and the archive of the European Southern Observatory. The final data products are made available by contacting the corresponding author.

REFERENCES

- Allard F., Hauschildt P. H., 1995, *ApJ*, 445, 433
- Astudillo-Defru N., Delfosse X., Bonfils X., Forveille T., Lovis C., Rameau J., 2017, *A&A*, 600, A13
- Bailer-Jones C. A. L., Rybizki J., Andrae R., Fouesneau M., 2018, *A&A*, 616, A37
- Baraffe I., Chabrier G., Barman T. S., Allard F., Hauschildt P. H., 2003, *A&A*, 402, 701
- Baraffe I., Homeier D., Allard F., Chabrier G., 2015, *A&A*, 577, A42
- Bensby T., Feltzing S., Lundström I., 2003, *A&A*, 410, 527
- Bentley J., Tinney C. G., Sharma S., Wright D., 2019, *MNRAS*, 490, 4107
- Beuzit J. L. et al., 2019, *A&A*, 631, A155
- Bonati I., Lichtenberg T., Bower D. J., Timpe M. L., Quanz S. P., 2019, *A&A*, 621, A125
- Bovy J., 2015, *ApJS*, 216, 29
- Brandt T. D., 2021, *ApJS*, 254, 42
- Cantalloube F. et al., 2015, *A&A*, 582, A89
- Carbillet M. et al., 2011, *Exp. Astron.*, 30, 39
- Carrión-González Ó., García Muñoz A., Santos N. C., Cabrera J., Csizmadia S., Rauer H., 2021, *A&A*, 651, A7
- Chen D.-C. et al., 2021, *ApJ*, 909, 115
- Coşkunoğlu B. et al., 2011, *MNRAS*, 412, 1237
- Cutri R. M. et al., 2003, VizieR Online Data Catalog, p. II/246
- Cutri R. M. et al., 2021, VizieR Online Data Catalog, p. II/328
- Dehnen W., Binney J. J., 1998, *MNRAS*, 298, 387
- Dieterich S. B., Henry T. J., Golimowski D. A., Krist J. E., Tanner A. M., 2012, *AJ*, 144, 64
- Dotter A., 2016, *ApJS*, 222, 8
- Douglas S. T., Agüeros M. A., Covey K. R., Cargile P. A., Barclay T., Cody A., Howell S. B., Kopytova T., 2016, *ApJ*, 822, 47
- ESA ed., 1997, The HIPPARCOS and TYCHO catalogues. Astrometric and photometric star catalogues derived from the ESA HIPPARCOS Space Astrometry Mission, ESA Publications Division, Noordwijk, NL
- Frankel N., Rix H.-W., Ting Y.-S., Ness M., Hogg D. W., 2018, *ApJ*, 865, 96
- Frankel N., Sanders J., Ting Y.-S., Rix H.-W., 2020, *ApJ*, 896, 15
- Gagné J. et al., 2018, *ApJ*, 856, 23
- Gaia Collaboration et al., 2016, *A&A*, 595, A1
- Gaia Collaboration et al., 2021, *A&A*, 649, A1
- Gravity Collaboration et al., 2018, *A&A*, 615, L15
- Hosey A. D., Henry T. J., Jao W.-C., Dieterich S. B., Winters J. G., Lurie J. C., Riedel A. R., Subasavage J. P., 2015, *AJ*, 150, 6
- Kasdin N. J., et al., 2020, in Lystrup M., Perrin M. D., Batalha N., Siegler N., Tong E. C., eds, Space Telescopes and Instrumentation 2020: Optical, Infrared, and Millimeter Wave. Vol. 11443, Proc. SPIE Conf. Ser., SPIE, Bellingham, p. 114431U
- Kervella P., Arenou F., Thévenin F., 2022, *A&A*, 657, A7
- Kopytova T. G., Brandner W., Tognelli E., Prada Moroni P. G., Da Rio N., Röser S., Schillbach E., 2016, *A&A*, 585, A7
- Kuznetsov M. K., del Burgo C., Pavlenko Y. V., Frith J., 2019, *ApJ*, 878, 134
- Lam K. W. F. et al., 2021, *Science*, 374, 1271
- Lenzen R. et al., 2003, in Iye M., Moorwood A. F. M., eds, SPIE Conf. Ser. Vol. 4841, Instrument Design and Performance for Optical/Infrared Ground-based Telescopes. SPIE, Bellingham, p. 944
- Lindgren L. et al., 2018, *A&A*, 616, A2
- Maire A.-L. et al., 2016, in Evans C. J., Simard L., Takami H., eds, Proc. SPIE Vol. 9908, Ground-based and Airborne Instrumentation for Astronomy VI. SPIE, Bellingham, p. 990834
- Maire A. L. et al., 2020, *A&A*, 639, A47
- Maldonado J., Villaver E., Eiroa C., Micela G., 2019, *A&A*, 624, A94
- Malo L., Doyon R., Lafrenière D., Artigau É., Gagné J., Baron F., Riedel A., 2013, *ApJ*, 762, 88
- Mamajek E. E., 2012, *ApJ*, 754, L20
- Marois C., Lafrenière D., Doyon R., Macintosh B., Nadeau D., 2006, *ApJ*, 641, 556
- Martinez P., Dorrer C., Carpentier E. A., Kasper M., Boccaletti A., Dohlen K., Yaitskova N., 2009, *A&A*, 495, 363
- Milli J. et al., 2018, in Close L. M., Schreiber L., Schmidt D., eds, Proc. SPIE Vol. 10703, Adaptive Optics Systems VI. SPIE, Bellingham, p. 107032A
- Reiners A., Mohanty S., 2012, *ApJ*, 746, 43
- Riedel A. R., Blunt S. C., Lambrides E. L., Rice E. L., Cruz K. L., Faherty J. K., 2017, *AJ*, 153, 95
- Rodríguez D., 2016, dr-rodriguez/Kinematics-App: Stellar Kinematics v1.0, Zenodo, Available at: <https://doi.org/10.5281/zenodo.192159>
- Rousset G. et al., 2003, in Wizinowich P. L., Bonaccini D., eds, Proc. SPIE Vol. 4839, Adaptive Optical System Technologies II. SPIE, Bellingham, p. 140
- Sauvage J.-F. et al., 2016, Introduction to Adaptive Optics: Adaptive Optics Systems V. SPIE, Bellingham
- Soderblom D. R., 2010, *ARA&A*, 48, 581
- Soumer R., Sivaramakrishnan A., Pueyo L., Macintosh B., Oppenheimer B. R., 2011, *ApJ*, 729, 144
- Stelzer B., Marino A., Micela G., López-Santiago J., Liefke C., 2013, *MNRAS*, 431, 2063
- Suárez Mascareño A., Rebolo R., González Hernández J. I., Esposito M., 2015, *MNRAS*, 452, 2745
- Thompson R. I., Schneider G., 1998, in Bely P. Y., Breckinridge J. B., eds, Proc. SPIE Vol. 3356, Space Telescopes and Instruments V. SPIE, Bellingham, p. 215
- Trauger J., Moody D., Krist J., Gordon B., 2016, *J. Astron. Telescopes, Instrum. Syst.*, 2, 011013
- Trifonov T., Tal-Or L., Zechmeister M., Kaminski A., Zucker S., Mazeh T., 2020, *A&A*, 636, A74
- Vigan A., 2020, Astrophysics Source Code Library, record ascl:2009.002
- Winter A. J., Kruijssen J. M. D., Longmore S. N., Chevance M., 2020, *Nature*, 586, 528
- Zari E., Hashemi H., Brown A. G. A., Jardine K., de Zeeuw P. T., 2018, *A&A*, 620, A172

This paper has been typeset from a $\text{\TeX}/\text{\LaTeX}$ file prepared by the author.